



UNIVERSITY OF LEEDS

This is a repository copy of *Large eddy simulation of inertial fiber deposition mechanisms in a vertical downward turbulent channel flow*.

White Rose Research Online URL for this paper:
<http://eprints.whiterose.ac.uk/113899/>

Version: Accepted Version

Article:

Njobuenwu, DO orcid.org/0000-0001-6606-1912 and Fairweather, M (2017) Large eddy simulation of inertial fiber deposition mechanisms in a vertical downward turbulent channel flow. *AIChE Journal*, 63 (4). pp. 1451-1465. ISSN 0001-1541

<https://doi.org/10.1002/aic.15664>

© 2017 American Institute of Chemical Engineers. This is the peer reviewed version of the following article: Njobuenwu, D. O. and Fairweather, M. (2017), Large eddy simulation of inertial fiber deposition mechanisms in a vertical downward turbulent channel flow. *AIChE J.*, 63: 1451–1465. doi:10.1002/aic.15664, which has been published in final form at <https://doi.org/10.1002/aic.15664>. This article may be used for non-commercial purposes in accordance with Wiley Terms and Conditions for Self-Archiving. Uploaded in accordance with the publisher's self-archiving policy.

Reuse

Unless indicated otherwise, fulltext items are protected by copyright with all rights reserved. The copyright exception in section 29 of the Copyright, Designs and Patents Act 1988 allows the making of a single copy solely for the purpose of non-commercial research or private study within the limits of fair dealing. The publisher or other rights-holder may allow further reproduction and re-use of this version - refer to the White Rose Research Online record for this item. Where records identify the publisher as the copyright holder, users can verify any specific terms of use on the publisher's website.

Takedown

If you consider content in White Rose Research Online to be in breach of UK law, please notify us by emailing eprints@whiterose.ac.uk including the URL of the record and the reason for the withdrawal request.



eprints@whiterose.ac.uk
<https://eprints.whiterose.ac.uk/>

Large eddy simulation of inertial fibre deposition mechanisms in a vertical downward turbulent channel flow

Derrick O. Njobuenwu* and Michael Fairweather

School of Chemical and Process Engineering, University of Leeds, Leeds, LS2 9JT, UK

Abstract

The deposition pattern of elongated inertial fibres in a vertical downward turbulent channel flow is predicted using large eddy simulation and Lagrangian particle tracking. Three dominant fibres deposition mechanisms are observed, namely, diffusional deposition for small inertial fibres, free-flight deposition for large inertial fibres, and the interception mechanism for very elongated fibres. The fibres are found to exhibit orientation anisotropy at impact, which is strongly dependent on the fibre elongation. An increase in the fibre elongation increases the wall capture efficiency by the interception mechanism. The diffusional deposition mechanism is shown to dominate for fibres with large residence time, t_{res}^+ , in the accumulation zone and small deposition velocities, v_z^+ , while the free-flight mechanism governs deposition for fibres with small t_{res}^+ and large v_z^+ . This study describes how particles deposit on a surface and, ultimately for many practical applications, how such deposition may promote fouling.

Topical Heading: Transport Phenomena and Fluid Mechanics

Keywords. Large eddy simulation, fibre deposition, fibre orientation, fibre-wall interaction, turbulent flow

* Corresponding author. Tel: +44113-343-2351
Email address: d.o.njobuenwu@leeds.ac.uk (D.O. Njobuenwu)

Introduction

Turbulent flows with suspended solid particles are found in many engineering, industrial and environmental situations. Determination of the rate and mechanisms of particle dispersion and deposition on solid surfaces is also of great importance because of their impact in practical applications. Examples of such include the deposition of corrosion oxides in the form of CRUD (corrosion residual unidentified deposits) in nuclear reactors ¹, the fouling of heat exchangers and turbine blades ², targeted pharmaceutical drug delivery, and aerosol deposition in the respiratory tract. In the case of nuclear reactor applications, of particular interest here, in-circuit corrosion products arising from metal surfaces exposed to gaseous coolant are small in size, but these can agglomerate into larger particles giving rise to a wide range of sizes and shapes which can eventually deposit on the boiler tubes or fuel cladding, creating concerns that impact on safety, thermal efficiency and fuel performance ¹.

Particles are transferred by turbulent sweeps into the wall region, where they preferentially segregate into elongated clusters which correlate well with the instantaneous position of low speed streaks at the wall, whereas ejections transfer particles from the wall region to the outer flow ³. Inertial effects largely depend on the characteristic time scales between the particle and fluid phases, usually represented by a dimensionless number, namely the particle Stokes number $St = \tau_p / \tau_f$, where τ_p is the particle relaxation time and τ_f is a flow characteristic time. Preferential concentration is at a maximum when the particle relaxation time is comparable to the Kolmogorov time, $\tau_f = \tau_\eta = \eta^2 / \nu$ ⁴, where η is the Kolmogorov length scale and ν the kinematic viscosity.

Particle deposition, defined here as the process of attaching suspended particles from a fluid in motion to the surface of a sticky wall, correlates well with the interaction of coherent turbulent structures (sweeps and ejections) with particle inertia ⁴⁻⁷. Two deposition mechanisms are usually referred to. The fluid's large-scale turbulent eddies are sufficiently

energetic to rapidly transport particles from the core region of a flow to the near-wall region where the local coherent structures dominate the particle-fluid interactions ⁴. For large, high-inertia particles, $\tau_p^+ \gg 1$, the large-scale eddies are strong enough to carry the particles through the accumulation region and deposit them by impaction directly at the wall. In such cases the dominant deposition process is known as the free-flight mechanism ^{6,7}, or inertial impaction ⁸, and the particles deposit with large velocities and small near-wall residence times. In contrast, particles with small inertia may be trapped in the wall region or re-entrained into the outer flow. Particles driven to the wall by sweep events and not re-entrained in the outer flow by ejections are bound to remain in the viscous wall layer, and accumulate in specific flow regions, not far from the wall, with long residence times ⁴. Such particles may eventually deposit with negligible velocities under the action of turbulent fluctuations. The dominant deposition process in this case is the diffusional mechanism ⁷.

Based on the particle inertia and the turbulent coherent structures, a universal deposition curve ($u_d^+ - \tau_p^+$) can be constructed in which three distinct deposition regimes are present ^{5,8,9}. In regime 1, sub-micron particle ($\tau_p^+ < 1$) deposition is effected by a combination of Brownian and eddy diffusion. The particle deposition velocity u_d^+ slowly decreases with an increase in the particle response time τ_p^+ . In regime 2, micron-sized particles ($0.1 \leq \tau_p^+ < 10$) deposit as a consequence of turbulent diffusion and impaction due to the growing particle inertia. The particle deposition velocity increases steeply with increases in the particle response time in this regime. The deposition of larger particles ($\tau_p^+ > 10$) is mainly by impaction due to particle inertia. This regime, regime 3, is characterised by a slow decrease in the particle deposition velocity as the particle response time increases.

Most of the early numerical modelling of particle deposition in wall-bounded, vertical turbulent flows adopted the Eulerian-Lagrangian framework using computational fluid

dynamic (CFD) approaches to predict the flow field. In many cases, the CFD approaches adopted a Reynolds-averaged Navier-Stokes (RANS) methodology with various turbulence models for the carrier phase and Lagrangian particle tracking (LPT), with various particle dispersion models, for the particle phase. These methods are frequently used due to their low computational cost and ease of application. However, they tend to over-predict by several orders of magnitude the particle deposition rate when considered against benchmark data ⁵ in regimes 1 and 2, that is for very small particles and for high Reynolds number flows. To obtain higher levels of accuracy when predicting particle deposition, especially in regimes 1 and 2, flow field predictions obtained from direct numerical simulation (DNS) or large eddy simulation (LES) are required. DNS coupled to LPT has been used successfully to predict particle dispersion and deposition in vertical turbulent channel flows, e.g. ¹⁰⁻¹². LES together with sub-grid scale (SGS) velocity fluctuation contributions has also been used in the simulation of particle deposition in channel flows ¹²⁻¹⁵. Salmanzadeh et al. ¹⁴, and Njobuenwu and Fairweather ¹⁵, in particular observed that the inclusion of SGS turbulent fluctuations improves predictions of the particle deposition rate, especially for small particles.

Non-spherical particles in turbulent flows have been studied using a variety of physical modelling ^{3,16,17} as well as CFD approaches. For the CFD approaches, detailed information on the aerodynamic forces, e.g. drag force, acting on these particles is required ¹⁸. Recently, the drag force and the aerodynamic torque acting on non-spherical particles in CFD techniques, e.g. ¹⁹⁻²³, has been based on the Jeffery equation ²⁴⁻²⁶. Zastawny et al. ²⁷ recently showed that the behaviour of inertial non-spherical particles may not be accurately predicted using the Stokesian models put forward by Jeffery ²⁴ and Brenner ²⁶. Empirical and numerical correlations ^{18,27-30} have long been used to extend the drag forces in the Stokesian regime (particle Reynolds number less than unity) to investigate those forces in higher Reynolds number flows for both spherical and non-spherical particles. For the motion of spherical particles, common practice is to use empirical expressions that relate the particle Reynolds number and the drag coefficient, such as the Schiller and Naumann drag

expression. In using these empirical correlations for non-spherical particles, the departure in shape from a sphere is accommodated by the inclusion of an equivalent diameter, d_{ev} , as a geometric parameter and optionally a shape factor, e.g. sphericity Φ_s , together with particle orientation dependency in the drag correlations. Four approaches have been identified, as reviewed by Mandø and Rosendahl ³¹, which include those based on the work of Rosendahl ²⁹, Yin et al. ³², Hölzer and Sommerfeld ¹⁸ and the lattice Boltzmann method for modelling non-spherical particles at finite Reynolds number, $Re_p \gg 1$ ³³.

For the flows of interest, i.e. the transport of CRUD in nuclear reactors, the corrosion oxides are simulated as fibres and the nuclear reactor fuel pin is modelled simplistically as the walls of a channel flow. Our aim is to understand the mechanisms responsible for the fibre fluxes and their deposition pattern on the walls. We adopt LES over RANS and DNS as LES is now used for more industrial-orientated configurations and represents a compromise between accuracy and computational speed. We employ the method described in Yin et al. ³² originally developed for sedimentation of finite-length cylindrical particles in stagnant water. In Njobuenwu and Fairweather ³⁴, we extended the Yin et al. ³² approach to handle disks, needles, cylinders and fibres in turbulent flows. Further extension was in the accurate modelling of particle-wall interaction for ellipsoidal particles and in the inclusion of a generalised shear lift force model applicable to arbitrary particle shapes in arbitrary shear flows ²³. The inclusion of the shear lift force has been shown to improve the prediction of the deposition rate of spherical particles ¹⁵ and of non-spherical particles ³⁵ in wall-bounded turbulent flows.

Mathematical Model

Large eddy simulation

In large eddy simulation, a spatial filtering operation is used to separate the large scale (resolved) from the small scale (sub-grid) motions. The filtered continuity and Navier-Stokes equations are given as:

$$\text{Continuity:} \quad \frac{\partial \bar{u}_i}{\partial x_i} = 0, \quad (1)$$

$$\text{Navier-Stokes:} \quad \frac{\partial \bar{u}_i}{\partial t} + \bar{u}_j \frac{\partial \bar{u}_i}{\partial x_j} = -\frac{1}{\rho} \frac{\partial \bar{p}}{\partial x_i} - \frac{\partial}{\partial x_j} (\bar{\sigma}_{ij} + \tau_{ij}), \quad (2)$$

where $\bar{\sigma}_{ij} = -2\nu\bar{s}_{ij}$, ρ , u_j and p represent the viscous stress, density, velocity and pressure of the fluid, respectively, $\bar{s}_{ij} = \frac{1}{2}(\partial\bar{u}_i/\partial x_j + \partial\bar{u}_j/\partial x_i)$ is the filtered strain-rate tensor, and ν is the kinematic viscosity. The sub-grid scale tensor $\tau_{ij} = \overline{u_i u_j} - \bar{u}_i \bar{u}_j$ is computed using the dynamically calibrated version of the Smagorinsky model³⁶.

The results presented below were obtained using the block-structured, boundary conforming coordinate LES code, BOFFIN³⁷. The code is based on a finite-volume approach using an implicit low-Mach number formulation with a two-step approximate factorisation pressure correction technique used to ensure mass conservation. All spatial derivatives are approximated with second-order central differences and a Crank-Nicolson scheme is used for temporal discretisation. The time step is chosen by requiring that the maximum Courant number lies between 0.1 and 0.3. Further details of the method and solution algorithm can be found in³⁷.

In the present work, simulations were performed at a shear Reynolds number, $Re_\tau = hu_\tau/\nu = 300$, where $u_\tau = (\langle \tau_w \rangle / \rho)^{0.5}$ is the shear velocity with $\langle \tau_w \rangle$ the time- and space-averaged wall shear stress, and h the channel half-height. Simulations were carried

out using air with a density $\rho = 1.3 \text{ kg m}^{-3}$ and a kinematic viscosity $\nu = 1.57 \times 10^{-5} \text{ m}^2\text{s}^{-1}$. The channel axes used were $(x \times y \times z)$, the domain size was set to $(2h \times \pi h \times 2\pi h)$ and the grid nodes employed were $129 \times 128 \times 128$ in the wall-normal, spanwise and streamwise directions, respectively. Periodic boundary conditions were imposed in the streamwise and spanwise directions, while the no-slip condition was enforced at the walls. Grid points were uniformly distributed in both the y and z directions, with non-uniform spacing in the wall-normal (x) direction.

Lagrangian particle equation of motion

Kinematics

Non-spherical particles were modelled in the present work using super-quadratic ellipsoid forms where more than one reference frame, as shown in Fig. 1(a), is needed to model the particle dynamics. The equations for translational motion are expressed in the fixed (inertial) frame $\mathbf{x} = [x, y, z]$, while rotational motions are considered in the particle frame $\mathbf{x}' = [x', y', z']$. A third frame of reference is $\mathbf{x}'' = [x'', y'', z'']$, which is the co-moving frame with its origin coinciding with the particle centroid and its axes being parallel to the fixed frame of reference. The transformation between the co-moving frame and the particle frame is expressed as $\mathbf{x}' = \mathbf{A}\mathbf{x}''$, where $\mathbf{A} = [a_{ij}]$ is the transformation matrix, whose elements represent the four Euler quaternions $\mathbf{q} = [q_0, q_1, q_2, q_3]^T$.

The orientational matrix is given as:

$$\mathbf{A} = \begin{bmatrix} 1 - 2(q_2^2 + q_3^2) & 2(q_1q_2 + q_0q_3) & 2(q_1q_3 - q_0q_2) \\ 2(q_1q_2 - q_0q_3) & 1 - 2(q_1^2 + q_3^2) & 2(q_2q_3 + q_0q_1) \\ 2(q_1q_3 + q_0q_2) & 2(q_2q_3 - q_0q_1) & 1 - 2(q_1^2 + q_2^2) \end{bmatrix}, \quad (3)$$

where the individual quaternions are obtained from the three Euler angles (φ, θ, ψ) as:

$$\begin{aligned}
q_0 &= \cos \frac{\varphi + \psi}{2} \cos \frac{\theta}{2}, & q_1 &= \cos \frac{\varphi - \psi}{2} \sin \frac{\theta}{2}, \\
q_2 &= \sin \frac{\varphi - \psi}{2} \sin \frac{\theta}{2}, & q_3 &= \cos \frac{\varphi + \psi}{2} \cos \frac{\theta}{2}.
\end{aligned} \tag{4}$$

The time evolution of the quaternions is used to update the orientation of the particles and is computed as:

$$\frac{d\mathbf{q}}{dt} = \begin{pmatrix} \dot{q}_0 \\ \dot{q}_1 \\ \dot{q}_2 \\ \dot{q}_3 \end{pmatrix} = \frac{1}{2} \begin{bmatrix} q_0 & -q_1 & -q_2 & -q_3 \\ q_1 & q_0 & -q_3 & q_2 \\ q_2 & q_3 & q_0 & -q_1 \\ q_3 & -q_2 & q_1 & q_0 \end{bmatrix} \begin{bmatrix} 0 \\ \omega_x \\ \omega_y \\ \omega_z \end{bmatrix}. \tag{5}$$

The position of the centre of mass of a particle, \mathbf{x}_p , depends on the particle velocity, \mathbf{v} :

$$\frac{d\mathbf{x}_p}{dt} = \mathbf{v}. \tag{6}$$

Dynamics

The dynamics of the particle phase is influenced by the turbulent flow (i.e one-way coupling). The particle volume fraction is low enough to neglect particle-particle interactions and their feed-back to the fluid flow. A Lagrangian particle tracking technique is used in which the translational velocity of the particle is obtained from the equation:

$$\frac{d\mathbf{v}}{dt} = \mathbf{F}_D + \mathbf{F}_{PL} + \mathbf{F}_{BG} + \mathbf{F}_{SL} + \mathbf{X}_{SGS}, \tag{7}$$

where the terms on the right hand side of Eq. (7) are forces per unit mass which include the drag, profile lift force due to particle orientation, buoyancy-gravity and shear lift, and a stochastic term representing the influence of the SGS velocity fluctuations on the particle acceleration.

The drag force and the profile lift force acting on a single particle due to the particle orientation in Eq. (7) are expressed as ³²:

$$\mathbf{F}_D = \frac{1}{2} \rho A_D C_D |\mathbf{u} - \mathbf{v}| (\mathbf{u} - \mathbf{v}), \quad (8)$$

$$\mathbf{F}_{PL} = \frac{1}{2} \rho A_L C_L \frac{\mathbf{z}' \cdot (\mathbf{u} - \mathbf{v})}{|\mathbf{u} - \mathbf{v}|} [\mathbf{z}' \times (\mathbf{u} - \mathbf{v})] \times (\mathbf{u} - \mathbf{v}), \quad (9)$$

where $\mathbf{u} = [u_x, u_y, u_z]$ and $\mathbf{v} = [v_x, v_y, v_z]$ are the fluid and particle velocity vectors at the particle centroid, \mathbf{z}' in Eq. (9) is the direction of the particle major axis, and A_D and A_L are the particle projected areas normal to the direction of the drag and profile lift forces, respectively. The projected areas A_D and A_L are expressed as a function of the incidence angle, α_i , with the incidence angle being the angle between the slip velocity $|\mathbf{u} - \mathbf{v}|$ and particle major axis \mathbf{z}' , as shown in Fig. 1(b). This angle provides coupling between the translational and rotational motions:

$$A_D = \pi a^2 \left[\cos^2 \alpha_i + (4\lambda/\pi)^2 \sin^2 \alpha_i \right]^{\frac{1}{2}}, \quad (10)$$

$$A_L = \pi a^2 \left[\sin^2 \alpha_i + (4\lambda/\pi)^2 \cos^2 \alpha_i \right]^{\frac{1}{2}}, \quad (11)$$

where $A_D = A_L = \pi a^2$ for a spherical particle with aspect ratio $\lambda = c/a = 1.0$. The drag coefficient, C_D , in Eq. (8) is obtained from a correlation for non-spherical particles available in the literature for particle Reynolds numbers beyond the Stokes regime ($Re_p \gg 1$). The Ganser²⁸ drag coefficient correlation is adopted and modified with the particle projected area, A_D , the incidence angle, α_i , and the particle equivalent sphere diameter:

$$\frac{C_D}{C_C K_2} = \frac{24}{Re_p K_1 K_2} \left[1 + 0.118 (Re_p K_1 K_2)^{0.6567} \right] + \frac{0.4305}{1 + 3305 / (Re_p K_1 K_2)}, \quad (12)$$

where $Re_p = |\mathbf{u} - \mathbf{v}| d_{ev} / \nu$ is the particle Reynolds number, $K_1 = (\frac{1}{3} d_n / d_{ev} + \frac{2}{3} \Phi_s^{-0.5})$ and $K_2 = 10^{1.8148(-\log \Phi_s)^{0.5743}}$ are the Stokes and Newton shape factors that model the particle sphericity and orientation, $d_n = (4A_D / \pi)^{0.5}$ is the equal-projected area circle diameter, and $\Phi_s = s/S$ is the particle sphericity, defined as the ratio of the surface area of a sphere

having the same volume as the particle, s , to the actual surface area of the non-spherical particle, S .

Following recent findings^{31,38}, the profile lift coefficient, C_L in Eq. (9), is determined such that the ratio of the lift to drag forces is a function of the particle incidence angle and the Reynolds number of the cross-flow³¹:

$$\frac{C_L}{C_D} = \frac{\sin^2 \alpha_i \cos \alpha_i}{0.65 + 40 \text{Re}^{0.72}}. \quad (13)$$

The buoyancy-gravity force, \mathbf{F}_{BG} in Eq.(7), is given by:

$$\mathbf{F}_{BG} = \mathbf{g}(1 - \Phi_\rho^{-1}), \quad (14)$$

where $\Phi_\rho = \rho_p / \rho$ is the ratio of the particle to fluid density and \mathbf{g} is the gravitational acceleration vector.

The shear lift force for a sphere in an arbitrary shear flow was obtained by extending the Saffman lift force for a sphere, where only one component of the velocity gradient tensor $\partial u_i / \partial x_j$ is non-zero, by introduction of the fluid rotation, $\boldsymbol{\Omega} = 0.5 \nabla \times \mathbf{u}$. Ravnik et al.²³ proposed a generalised lift tensor for an arbitrary shape in an arbitrary shear equivalent to the Crowe et al.³⁹ generalised shear lift force for spheres. The modified version of the Ravnik et al.²³ shear lift force for arbitrary shapes in an arbitrary shear was used in the simulations.

The stochastic term, \mathbf{x}_{SGS} , in Eq.(7) is written as the product of the diffusion coefficient matrix and the increment of the Wiener process, $d\mathbf{W}_t$:

$$\mathbf{x}_{SGS} = \left(C_0 \frac{k_{sgs}}{\tau_t} \right)^{0.5} \frac{d\mathbf{W}_t}{dt}, \quad (15)$$

where C_0 is a model constant whose value has been provisionally assigned ³⁷, and $d\mathbf{W}_i$ in Eq. (15) represents the increment of the Wiener process. During the simulation, the increment of the Wiener process, $\Delta\mathbf{W}_i/\Delta t$, was represented by $\xi_i \times (\Delta t)^{-0.5}$, where ξ_i is a random vector sampled from a standardised Gaussian distribution, independent for each time step and for each velocity component. τ_t in Eq. (15) is a sub-grid time scale which determines the rate of interaction between the particle and carrier phase turbulence and it is given in Bini and Jones ³⁷ as:

$$\tau_t = \frac{(\tau_p f_D)^{2\alpha}}{(\Delta / \sqrt{k_{sgs}})^{2\alpha-1}}, \quad (16)$$

The SGS kinetic energy, k_{sgs} , is obtained using equilibrium arguments from:

$$k_{sgs} = \left(2\Delta v_{sgs} \overline{S_{ij} S_{ij}}\right)^{\frac{2}{3}}, \quad (17)$$

The particle relaxation time is given as $\tau_p = \rho_p d_p^2 / 18\mu$ for a spherical particle with diameter, d_p , however, for ellipsoidal particles, a common approach is to transform the particle size to sphere-equivalent particles, known as the effective diameter method. Several modifications are available for ellipsoidal particle diameter and response time ²², with the equivalent volume-of-sphere diameter, $d_{ev} = 2a\lambda^{1/3}$, adopted in this work. The particle response time for ellipsoidal particles based on the equivalent volume-of-sphere diameter, d_{ev} , becomes $\tau_{ev} = \rho_p d_{ev}^2 / 18\mu$, and as for the particle Stokes number:

$$\tau_{ev}^+ = \frac{\tau_{ev}}{\tau_f} = \frac{d_{ev}^{+2} \Phi_{\rho}}{9}. \quad (18)$$

The rotational motion of an ellipsoid about its principal axes is given by Euler's equation as:

$$\begin{aligned}
\frac{d\omega_{x'}}{dt} &= \frac{T_{x'}}{I_{x'x'}} + \left(\frac{I_{y'y'} - I_{z'z'}}{I_{x'x'}} \right) \omega_{y'} \omega_{z'} \\
\frac{d\omega_{y'}}{dt} &= \frac{T_{y'}}{I_{y'y'}} + \left(\frac{I_{z'z'} - I_{x'x'}}{I_{y'y'}} \right) \omega_{z'} \omega_{x'} \\
\frac{d\omega_{z'}}{dt} &= \frac{T_{z'}}{I_{z'z'}} + \left(\frac{I_{x'x'} - I_{y'y'}}{I_{z'z'}} \right) \omega_{x'} \omega_{y'}
\end{aligned} \tag{19}$$

The principal moments of inertia of a spheroid are $I_{x'x'} = I_{y'y'} = \frac{1}{5} m_p a^2 (1 + \lambda^2)$ and $I_{z'z'} = \frac{2}{5} m_p a^2$.

The net torque acting on the particle is $\mathbf{T} = \mathbf{T}_H + \mathbf{T}_R$. \mathbf{T}_H is the torque due to non-coincidence of centres of gravity (CG) and pressure (CP) and is a function of the hydrodynamic force, as illustrated in Fig. 1(b). The aerodynamic forces act at CP which is located a distance x_{cp} from CG. Using the particle major axis, \mathbf{z}' , and the transformation matrix, \mathbf{A} , \mathbf{T}_H is given in the particle frame of reference as ³²:

$$\mathbf{T}_H = \mathbf{A}[(x_{cp} \mathbf{z}') \times (\mathbf{F}_D + \mathbf{F}_L)], \tag{20}$$

where

$$x_{cp} = 0.25c(1 - e^{3(1-\lambda)}) |\cos^3 \alpha_i|, \tag{21}$$

which is based on a semi-empirical expression proposed in ³². The components of torque due to the resistance on a rotating body, $\mathbf{T}_R = [T_{x'}, T_{y'}, T_{z'}]$, acting on the ellipsoidal particles are given as ⁴⁰:

$$T_{x'} = \frac{16\pi\mu a^3 \lambda}{3(\beta_0 + \lambda^2 \gamma_0)} [(1 - \lambda^2) d_{z'y'} + (1 + \lambda^2)(\omega_{z'y'} - \Omega_{x'})], \tag{22}$$

$$T_{y'} = \frac{16\pi\mu a^3 \lambda}{3(\alpha_0 + \lambda^2 \gamma_0)} [(\lambda^2 - 1) d_{x'z'} + (1 + \lambda^2)(\omega_{x'z'} - \Omega_{y'})], \tag{23}$$

$$T_{z'} = \frac{32\pi\mu a^3 \lambda}{3(\alpha_0 + \beta_0)} (\omega_{y'x'} - \Omega_{z'}), \tag{24}$$

where $d_{z'y'}$ and $d_{x'z'}$ are elements of the deformation rate tensor and $\omega_{z'y'}$, $\omega_{x'z'}$ and $\omega_{y'x'}$ are elements of the spin tensor in the particle frame. The non-dimensional coefficients α_0 , β_0 and γ_0 for a prolate ellipsoid ($\lambda > 1$) are defined as:

$$\alpha_0 = \beta_0 = \frac{\lambda^2}{\lambda^2 - 1} + \frac{\lambda}{2(\lambda^2 - 1)^{3/2}} \ln \left(\frac{\lambda - \sqrt{\lambda^2 - 1}}{\lambda + \sqrt{\lambda^2 - 1}} \right), \quad (25)$$

$$\gamma_0 = \frac{2}{\lambda^2 - 1} + \frac{\lambda}{(\lambda^2 - 1)^{3/2}} \ln \left(\frac{\lambda - \sqrt{\lambda^2 - 1}}{\lambda + \sqrt{\lambda^2 - 1}} \right). \quad (26)$$

Note that further details of the validity and limitations of the equations used for the non-spherical particle dynamic motion in the inertial frame are reported elsewhere ^{31,38,41,42}.

Ellipsoidal particle-wall collision model

A particle is considered to collide with the wall as soon as any of its surface touches the wall. For a spherical particle ($\lambda = 1$), this happens when the distance from its centroid to the wall surface is smaller than its radius ($x_p \leq a$). However, for an ellipsoidal particle this happens when the distance of its centroid to the wall lies between the semi-minor axis, a , and the semi-major axis, c , depending on the particle orientation. The probability of an ellipsoidal particle colliding with the wall therefore depends both on the distance of its centroid from the wall surface and its orientation relative to the wall. During initial simulations before statistics were taken, once a collision was detected, the particle was reflected elastically back into the flow. In such cases, the particle linear momentum in the wall-normal direction is changed in sign, whereas the linear momentum in the two homogenous directions and the angular momentum are unchanged ⁴¹. However, during deposition monitoring, all collisions resulted in deposition, mimicking a sticking wall. To find the touch point of an ellipsoid to a given arbitrary wall, a unit vector $[0, 0, 1]$ is attached to the ellipsoid major principle axis, the z' -axis in the particle frame, with the projection of this unit vector onto the local co-moving frame given by:

$$\mathbf{r}_{\text{rot}} = \mathbf{A}^T [0, 0, 1]^T, \quad (27)$$

and upon normalisation, the components of the orientation vector are given by:

$$\mathbf{x}_{rot} = \begin{bmatrix} x_{rot} \\ y_{rot} \\ z_{rot} \end{bmatrix} = \frac{2}{|\mathbf{r}_{rot}|} \begin{bmatrix} q_1 q_3 + q_0 q_2 \\ q_2 q_3 - q_0 q_1 \\ q_0^2 + q_3^2 - \frac{1}{2} \end{bmatrix}. \quad (28)$$

The ellipsoid length is defined as $L_p = 2a\lambda$, whereby the ellipsoid end points are located at:

$$\mathbf{x}_{endpoint} = \mathbf{x}_p \pm \frac{1}{2} L_p \mathbf{x}_{rot}, \quad (29)$$

A fourth order Runge-Kutta scheme was applied to solve the Newton equation of motion to give the particle position and velocity, and the Euler equation of rotation was solved to yield the particle orientation and rotation. Gravity was assumed to act along the direction of the flow (vertically downward). The particle to fluid density ratio was set to $\Phi_p = 770$, which represents the density ratio used in the experiments of Liu and Agarwal⁵ whose data conform to the universal deposition curve, and is as used in the computations of Marchioli and Soldati⁴³. Two hundred thousand particles for each fibre set (r_{ev}^+, λ) were uniformly distributed in the channel, with their initial linear and rotational velocity equal to those of the fluid at the particle position. The injected particle number was large enough to guarantee that the deposition results are independent of the initial number of particles injected. The particle initial orientation was specified randomly by Euler angles :

$$\begin{aligned} \varphi_0 &= 2\pi\xi_\varphi \\ \theta_0 &= \cos^{-1}(1 - \xi_\theta) \\ \psi_0 &= 2\pi\xi_\psi, \end{aligned} \quad (30)$$

where ξ_i is a random number with a uniform distribution between 0 and 1. Sufficient time (four eddy turnover times) was allowed for the particles to equilibrate within the flow before taking statistics.

Results and Discussion

Single Phase Velocity Statistics

First, the LES results for the fully developed turbulent channel flow at a shear Reynolds number of $Re_\tau = 300$, which corresponds to that used in the work of Marchioli and Soldati⁴³ and Liu and Agarwal⁵, are analysed. Time- and space-averaged results, in terms of the resolved velocities, are compared with the corresponding DNS results of Marchioli and Soldati⁴³ in Fig. 2. The mean streamwise velocity normalised by the wall variables (velocity scale, u_τ , and length scale, ν/u_τ), u_z^+ , is presented in Fig. 2(a). The root mean square of the velocity fluctuations normalised by the wall variables in the wall-normal, $u_{x,rms}^+$, spanwise, $u_{y,rms}^+$, and streamwise, $u_{z,rms}^+$, directions, and the Reynolds shear stress with respect to the streamwise and wall-normal directions normalised by the wall variables, $u_x'^+ u_z'^+$, are presented in Fig. 2(b). The comparisons show good agreement between the present results and those of the DNS, largely due to the highly resolved LES performed and the dynamic calibration of the Smagorinsky constant used.

A wide range of non-dimensional particle response times ($1 \leq \tau_{ev}^+ \leq 100$), particle aspect ratios ($1.001 \leq \lambda \leq 50$) and particle dynamic properties (wall-normal position, velocity and slip velocity, residence time, directional cosines) are considered in analysing the deposition process as the controlling mechanism changes from turbulent diffusion dominated, as is the case for very low inertia particles, to the unidirectional non-turbulent trajectories associated with high inertia particles. Selected relevant fibre simulation parameters are listed in Table 1. Particles with response times smaller than unity ($\tau_{ev}^+ < 1$) were not considered because it is difficult and computationally expensive to obtain representative statistical measures since there are fewer depositing particles for such very small particle inertia. The particle inertias considered fall within regimes 2 and 3 based on the universal $(u_d^+ - \tau_p^+)$ curve of deposition

regimes, as noted in ^{5,8}. For the sake of brevity and unless otherwise stated, the elongation is classified into three categories, viz, small elongation, $\lambda=1.001$, moderate elongation $\lambda=3-10$ and large elongation, $\lambda=30-50$.

Spatial and Orientation Distributions of Deposited Fibres

To understand the deposition pattern of fibres in wall-bounded turbulent flow, the distribution and orientation of fibres with selected particle parameters $(\tau_{ev}^+, \lambda) = (5, 10)$, $(25, 3)$ and $(25, 10)$ that have deposited on one wall of the channel flow are shown in Fig. 3(a), (b) and (c), respectively. To aid clarity, the fibre size has been scaled-up 70 times relative to the scale of the $y-z$ plane. The fibres deposited on the $y-z$ plane are coloured, with the scale indicating the value of the absolute direction cosine, $|\cos\theta_x|$, between the particle principal axis, \mathbf{z}' , and the channel wall-normal direction (the global x -axis), where θ_x is defined in Fig. 1(c). The maximum value $|\cos\theta_x|=1$, coloured red, represents fibres aligned parallel to the wall-normal direction (x -axis), while the minimum value $|\cos\theta_x|=0$, coloured blue, represents fibres aligned across (or perpendicular to) the same wall-normal direction. Conversely, a fibre aligned parallel to the wall-normal direction will at the same time be aligned perpendicular to the flow direction (z -axis), and a fibre aligned perpendicular to the wall-normal direction will align parallel to the flow direction (z -axis). The figure shows qualitatively that fibre spatial and orientation distributions at the instance of deposition on the wall surface are highly dependent on the fibre's inertia, aspect ratio and the interplay between underlying turbulence and gravity.

In terms of the fibre distribution, there exists some local particle clustering for the selected particle parameter space $(\tau_{ev}^+, \lambda) = (5, 10)$, $(25, 3)$ and $(25, 10)$, as shown in Fig. 3, but no fibre streaks (i.e. regions of dense and sparse fibre numbers). With reference to the fibre's properties listed in Table 1, the selected fibres shown in Fig. 3 only deposit on the wall when

the location of the fibres' centre of mass in the wall-normal direction fulfils the deposition condition noted earlier. This means that fibre deposition occurs from within the viscous sub-layer region, which is the region where the fibres are trapped before depositing on the wall. Previous results show that fibre-streaks scale in the same manner as the viscous sub-layer streaks in a turbulent wall bounded flow, which is smaller in size when compared to clustering sizes in the buffer region. Hence, the degree of fibre clustering shown in this figure is not as pronounced as that reported in other studies^{4,19-21,34}, where strong clustering was observed for spheres and fibres around the buffer region and in turbulent flows without gravity. Additionally, the fibre distributions shown in Fig. 3 were not obtained from an instantaneous snapshot, but for all deposited particles noted over the entire sampling time interval. In this figure only about 3500 fibres are shown to aid visualization, although the results show that the number of deposited fibres increases with the fibre non-dimensional response time, which is consistent with particle deposition in regime 2 of the universal curve of deposition regimes^{5,8}, where the particle deposition velocity steadily increases with the response time. Fibre behaviour is further considered quantitatively below.

Mechanism of Fibre Deposition

To quantitatively analyse the role of fibre elongation and inertia on the deposition pattern of particles in a wall-bounded vertical turbulent flow, the probability density function (PDF) of the position of the particle centre of mass along the wall-normal direction at impact, normalised by the length of the particle semi-minor axis, a , and semi-major axis, c , is examined. The PDF is computed using $f(\xi) = N_\xi / N$, where $\xi = \phi_i$, with ϕ_i being the i^{th} variable of interest. Here, N_ξ is the number of fibres with ξ being the bin $[\xi, \xi + \Delta\xi]$ and $\Delta\xi = (\xi_{\max} - \xi_{\min}) / N_B$. N is the total number of samples used and N_B is the number of bins.

The results of Fig. 4 show that both particle shape and inertia are parameters that influence the mechanism of particle deposition on the walls of a turbulent channel flow. Towards the extreme left of the abscissa in Fig. 4 deposition occurs with the fibre lying parallel to the wall (y - z plane), while towards the extreme right of the abscissa deposition occurs with the fibre standing perpendicular to the wall. Within these two limits, the probability of a fibre colliding with the wall depends on the distance of its centre of mass from the wall surface and its orientation relative to the wall. From a qualitative viewpoint the PDF is similar for each fibre inertia, i.e. in Fig. 4(a) and (b) for small inertia, in Fig. 4(c) and (d) for intermediate inertia, and in Fig. 4(e) and (f) for large inertia. For the $Re_\tau = 300$ flow, prolate particles with aspect ratio $\lambda < 10$ for all inertia ranges ($\tau_{ev}^+ = 1-100$) considered deposit on the wall when their centre of mass is within the viscous sub-layer, while for more elongated particles, the position of the centre of mass falls in the viscous sub-layer and part of the buffer layer (within 11 wall units from the lower wall). The left and right hand extremes of the horizontal axis in Fig. 4 show when the distance of the particle centre of mass from the surface is equal to the semi-minor axis, a , and the semi-major axis, c , respectively.

Fig. 4(a) and (b) show that the influence of the particle shape (in terms of its elongation) on its deposition pattern is weak and seemingly non-existent for fibres with small response times, $\tau_{ev}^+ = 1$ and $\tau_{ev}^+ = 5$. All fibres ($\lambda = 1.001, 3, 10, 30$ and 50) exhibit a similar trend, with a high probability of depositing with the smaller semi-minor axis being the leading edge rather than the semi-major axis, with a single peak in the PDF($(x-a)/(c-a)$) ~ 0 . This implies that most of the fibres with small inertia are able to travel through the viscous sub-layer region and deposit on the wall with an orientation which aligns its principal axis parallel to the wall surface. As the fibre inertia increases from small to intermediate ($\tau_{ev}^+ = 15$ and 25) in Fig. 4(c) and (d), and large ($\tau_{ev}^+ = 50$ and 100) in Fig. 4(e) and (f), in addition to the peak in the PDF($(x-a)/(c-a)$) ~ 0 , a secondary peak appears around $(x-a)/(c-a) = 0.8$ for all fibre aspect ratios, apart from the near-spherical case. This implies that as the fibre

elongation increases with an increase in the fibre size, deposition by the interception mechanism becomes more dominant. The interception mechanism increases in importance with increases in the fibre aspect ratio, with the fibre with the largest aspect ratio, $\lambda = 50$, showing the largest secondary peak at $(x - a)/(c - a) \approx 0.8$, while the least elongated, $\lambda = 3$, fibre shows the smallest secondary peak, apart from the near-spherical fibre which shows no secondary peak at all. This demonstrates that very elongated fibres, more than the least elongated fibres with equal inertia, deposit due their leading edge touching the wall. Hence, fibres with large aspect ratios have a higher deposition rate when compared with the near-spherical particles with equal non-dimensional equivalent response times, τ_{ev}^+ . This observation is consistent with that reported by Zhang et al. ⁴⁴.

Fig. 5 shows the PDF of the non-dimensional particle streamwise velocity, v_z^+ , at impact for varying fibre aspect ratios ($\lambda = 1.001, 3, 10, 30$ and 50) and for a range of non-dimensional particle response times. The magnitude of the velocity of the depositing particles towards the wall and the non-dimensional particle residence time, t_{res}^+ , shown in Fig. 6 are two parameters that are frequently used to describe the deposition mechanism as being due either to diffusional effects or attributable to the free-flight mechanism. Narayanan et al. ⁷ therefore categorised depositing particles into two regimes; those with large velocities towards the wall and small near-wall residence times were referred to as the free-flight population, whilst particles depositing with negligible velocities and with large near-wall residence times were referred to as the diffusional deposition population.

Fig. 5 follows the trend noted in Fig. 4 in terms of the similarity of the PDF for each fibre inertia range, i.e. in Fig. 5(a) and (b) for small inertia, Fig. 5(c) and (d) for intermediate inertia, and Fig. 5(e) and (f) for large inertia. For small fibre inertias shown in Fig. 5(a) and (b) for $\tau_{ev}^+ = 1$ and $\tau_{ev}^+ = 5$, a sharp peak in the PDF(v_x^+) is observed for all fibre aspect ratios, and at the lowest fibre velocity recorded. The observed value of the peak at $v_x^+ \sim 0.3$

for fibres with $\tau_{ev}^+ = 1$ in Fig. 5(a) reduces from a maximum in the PDF(v_x^+) ~ 0.42 for fibres with aspect ratio $\lambda = 1.001$ to PDF(v_x^+) ~ 0.20 for the most elongated fibres, $\lambda = 50$. As the fibre inertia is increased from $\tau_{ev}^+ = 1$ and $\tau_{ev}^+ = 5$ in Fig. 5(b), the relationship between the PDF peak and the particle aspect ratio changes from that seen in Fig. 5(a). Although the value of the PDF maximum remains at approximately 0.42, this occurs for an intermediate elongated fibre, $\lambda = 10$, with a shift in the location of the peak in the deposition velocity from $v_z^+ \sim 0.3$ to $v_z^+ \sim 0.4$. The magnitude of the deposition velocity increases with an increase in the fibre inertia across all aspect ratios, with the sharp peak in the PDF observed for small inertia fibres in Fig. 5(a) and (b) changing to a broader peak at higher velocities for the intermediate and large inertia fibres in Fig. 5 (c-f). The peak velocity is therefore seen to move from the left hand side of the abscissa to the right hand side for the near-spherical fibres, $\lambda = 1.001$, while the deposition velocity broadly increasing with an increase in the fibre aspect ratio.

Overall, increasing the particle inertia increases the fibre deposition velocity, while increasing the fibre aspect ratio increases the number of fibre depositions due to the interception mechanism, as shown in Fig. 5 and as discussed in relation to the results of Fig. 4. Note that there is a distinction between deposition velocity (i.e. the fibre velocity at the instant of deposition) and the deposition rate (i.e. the number of fibres deposited). Lastly, and in line with other works^{4,6,7}, it is concluded that fibres with small inertia and with a small deposition velocity are likely to deposit on the wall due to diffusional effects, whilst those with large inertia and a large deposition velocity are more likely to deposit on a wall via the free-flight mechanism. Elongated fibres, in addition to depositing through the diffusional or free-flight mechanisms, may also deposit on a wall due to the interception mechanism.

The PDF(t_{res}^+) of the time a fibre spends in the near-wall region, $x^+ < 5$, before it finally deposits on the wall surface is shown in Fig. 6, again for a range of non-dimensional particle

response times. To compute PDF(t_{res}^+) a time counter was initialised to zero for each particle entering the accumulation zone ($x^+ < 5$ and $x^+ > (Re_\tau - 5)$), and the counter was subsequently reinitialised to zero if a particle escaped from the accumulation zone before depositing due to re-entrainment into the bulk flow. Fibres already in the accumulation zone before sampling commenced were not considered in the particle residence time, t_{res}^+ . The time counter then stored the time a particle spent in the accumulation zone before its leading edge touched the wall surface. The particle residence time for all the deposited fibres was then analysed using a PDF. This analysis of the particle residence time was performed to corroborate the conclusions reached through use of the deposition velocity to classify the particle deposition mechanism. It also complements the earlier work by Narayanan et al. ⁷ who used a velocity-residence time plot to consider particle deposition. Narayanan et al. ⁷ defined free-flight deposition particles as particles having both a high deposition velocity and a short residence time, with diffusional deposition particles being those with very small deposition velocities and very large residence times. Based on the Narayanan et al. ⁷ classification, it is evident that there is a correlation between the fibres' inertia and the corresponding residence time preceding their deposition on the wall. The maximum fibre residence time reduces with an increase in the fibre inertia, with a maximum value of $t_{res}^+ \sim 850$ for $\tau_{ev}^+ = 1$ fibres in Fig. 6(a); $t_{res}^+ \sim 600$ for $\tau_{ev}^+ = 5$ fibres in Fig. 6(b); $t_{res}^+ \sim 340$ for $\tau_{ev}^+ = 15$ fibres in Fig. 6(c); $t_{res}^+ \sim 240$ for $\tau_{ev}^+ = 25$ fibres in Fig. 6(d); $t_{res}^+ \sim 170$ for $\tau_{ev}^+ = 50$ fibres in Fig. 6(e); and $t_{res}^+ \sim 150$ for $\tau_{ev}^+ = 100$ fibres in Fig. 6(f). Hence, the small inertia fibres with large residence times in Fig. 6(a) and (b), and small deposition velocities in Fig. 5(a) and (b), are depositing due to the diffusional deposition mechanism. On the other hand, the intermediate and large inertia fibres with small residence times in Fig. 6(c-f), and large deposition velocities in Fig. 5(c-f), are mostly likely depositing due to the free-flight deposition mechanism.

Fig. 6 also shows some correlation between the fibre aspect ratio and the residence time in characterising the fibre deposition mechanism in a turbulent flow. Fig. 6(a) and (b) show that the small inertia particles have an increasing residence time in the accumulation region when the aspect ratio increases from $\lambda = 1.001$ to $\lambda = 50$. The opposite trend is the case for the large inertia particles, Fig. 6(c-f), that deposit due to the free-flight mechanism, where in this case the fibres in general experience a decrease in residence time in the accumulation region with increasing aspect ratio. There is also some interplay between this deposition mechanism and the interception mechanism for the most elongated inertial fibres, hence, a shorted residence time was experienced by the largest fibre with $\tau_{ev}^+ = 100$, $\lambda = 50$.

The PDFs of the particle direction cosines, $\cos \theta_x$, $\cos \theta_y$ and $\cos \theta_z$, at the point of particle deposition on the wall surface are presented, respectively, in Figs. 7, 8 and 9 to again demonstrate the influence of fibre inertia and elongation on the fibre deposition pattern. These results elucidate how the fibre orientation in the near-wall region influences the deposition pattern, the understanding of which has relevance in a number of industrial applications. Note that the fibre principal (major) axis (z') is perpendicular to (or is aligned across) the global coordinates x , y or z axis when $\cos \theta_x = 0$, $\cos \theta_y = 0$ and $\cos \theta_z = 0$, and is parallel to (or aligned with) the same axes when $|\cos \theta_x| = 1$, $|\cos \theta_y| = 1$ and $|\cos \theta_z| = 1$. The fibre orientation angle, $\theta = [\theta_x, \theta_y, \theta_z]$, is defined as the angle between the fibre major axis, z' , and the global coordinates $\mathbf{x} = [x, y, z]$, as shown in Fig. 1(c). Henceforth, when discussing the orientation of the elongated particles, the major axis is implied.

In Figs. 7, 8 and 9, and as expected, the near-spherical particles for all inertias investigated mimic spherical particles and show no preferential alignment. Hence, the near-spherical fibres exhibit a flat and isotropic orientation profile irrespective of the fibre inertia. The orientation profile $\text{PDF}(|\cos \theta_x|)$, $\text{PDF}(|\cos \theta_y|)$ and $\text{PDF}(|\cos \theta_z|)$ for small fibre

inertias in Figs. 7(a) and (b), 8(a) and (b), and 9(a) and (b) are broadly different (except for the $\lambda = 1.001$ case) from those exhibited by the intermediate and large inertia fibres in Figs. 7(c-f), 8(c-f) and 9(c-f), suggesting again that different mechanisms dominate the deposition of fibres with small and with large inertia. For the small inertia fibres in Fig. 7(a), the fibres deposit on the wall aligning their principal axis, z' , perpendicular to the velocity gradient direction, x -axis, hence the PDF($|\cos \theta_x|$) peaks at 0 where $\theta_x = \pi/2$. This behaviour is seen to increase with increases in the fibre elongation, with the most elongated fibres, $\lambda = 30$ and 50, showing the highest peaks. When the fibre inertia is increased from $\tau_{ev}^+ = 1$ to $\tau_{ev}^+ = 5$ in Fig. 7(b), the fibres still exhibit a similar orientation to those in Fig. 7(a), but to a lesser degree. As the fibre inertia is increased further to the intermediate and large range, the fibres' principal axis, z' , switches from perpendicular to parallel alignment relative to the fluid velocity gradient direction (x -axis), therefore emphasising the effectiveness of fibre deposition by interception of the fibre leading edge. This behaviour is in line with that reported in the experimental studies of Kvasnak and Ahmadi¹⁶. With the interception effect increasing with fibre aspect ratio, it is clear that both the fibre inertia and the aspect ratio contribute significantly to the deposition process. The peak of the PDF($|\cos \theta_x|$) switches from being at $\theta_x = \pi/2$ to being at $\theta_x = 0$ and $\theta_x = \pi$, with the most elongated fibre, $\lambda = 50$, showing the largest peak. The observations of fibre orientation behaviour at impact with respect to the alignment of the principal axis with the wall-normal direction made in relation to Fig. 7 are further complemented by the results shown in Fig. 9.

With gravity having a negligible effect on fibres with the smallest inertia, results for fibres with the largest elongation therefore show that most are perpendicular to the plane of the channel wall. Since these fibres are within the viscous sub-layer at the point of deposition, their orientations are in contrast to those found by Mortensen et al.²⁰ and Marchioli et al.²¹ who also studied the orientation of ellipsoids and observed that fibres tend to align with the mean

flow near the wall (in the buffer region), while near the channel centre their orientation is approximately isotropic.

PDFs of fibre orientation in terms of the angle between the particle principal axis, z' , and the y -axis for aspect ratios $\lambda = 1.001-50$ and for non-dimensional equivalent response times $\tau_{ev}^+ = 1-100$ are shown in Fig. 8. The fibres with the smallest inertia, $\tau_{ev}^+ = 1-5$, and for the entire range of elongations investigated, are widely distributed, but with a preference to align across the spanwise axis (i.e. with the principle axis, z' , and the y -axis having an angle of $\pi/2$), as shown in Figs. 8(a) and (b) for $\tau_{ev}^+ = 1$ and $\tau_{ev}^+ = 5$, respectively. With increasing particle inertia ($\tau_{ev}^+ > 5$ in Figs. 8(c) to (f)), the fibre alignment observed for all aspect ratios of particles with inertia $\tau_{ev}^+ \leq 5$ reduces, and the fibre orientation with respect to the spanwise direction becomes more evenly distributed, with only a slight bias towards alignment across the spanwise direction. Differences in the distribution of the orientation state with respect to the spanwise axis between fibres with different aspect ratios are evident only at small particle inertia, $\tau_{ev}^+ \leq 5$, with the bias towards orientations perpendicular to the y -axis increasing slightly with aspect ratio. Overall, both the fibre inertia and elongation have a lesser effect on the variation of the orientation state of the particle principal axis with respect to the y -axis at the point of particle deposition on the wall surface than noted previously.

Lastly, the PDF($|\cos\theta_z|$) in Fig. 9(a) and (b) shows that the fibres with small inertia, $\tau_{ev}^+ = 1$ and $\tau_{ev}^+ = 5$, tend to align with the streamwise direction of the flow (z -axis) at the instant of impact with the wall, and these results are consistent with the fibre orientations shown in Fig. 7(a) and (b). Note that the orientation state of alignment with the x -axis ($|\cos\theta_x| = 1$) is the same as the alignment perpendicular to the z -axis and, conversely, alignment perpendicular to the x -axis is the same as the alignment with the z -axis ($|\cos\theta_z| = 1$). As the fibre inertia increases to $\tau_{ev}^+ = 15$, the strong alignment parallel to the streamwise direction of the flow

observed for small inertia disappears. Instead, there is transition between fibre alignment across and with the flow direction determined by a competition between the fibre inertia and the interception mechanism. Hence, the peak moves from $|\cos \theta_z| = 1$ in Fig. 9(a) and (b) to $|\cos \theta_z| = 0.5$ in Fig. 9(c) for $\tau_{ev}^+ = 15$ and for the fibres with small aspect ratios. The interplay between fibre inertia and elongation ensures a slight preferential alignment with the direction of the flow for higher inertia particles with large elongation. Broadly speaking, at moderate and large fibre inertia, alignment with the streamwise direction does not show a significant dependence on the fibre elongation, as seen in Fig. 9(c) to (f). This dispersive effect is enhanced with increasing τ_{ev}^+ , as a higher inertia means that the fibre is long enough to experience the turbulence inherent in the buffer region during its deposition on the wall surface. To some extent, fibres aligned across the flow direction show a broad distribution while those aligned with the direction of flow show a less broad distribution, for the high inertia particles at least.

Conclusions

The deposition of fibres with various elongations and inertia in a vertical channel flow was investigated using large eddy simulation and a Lagrangian particle tracking scheme coupled to the Euler rotation equation. The force balance adopted is comprised of deterministic and stochastic force terms that cater for the wide range of particle inertia and aspect ratios studied. Probability density functions were used to analyse the effects of fibre inertia and elongation on the fibre deposition mechanism in a turbulent vertical flow. The PDF of the wall-normal position of the fibre centre of mass, and those of the orientation of the fibre's principal axis, show that an increase in aspect ratio increases the wall capture efficiency by the interception mechanism. A relationship between fibre residence time, t_{res}^+ , in the accumulation zone and the fibre deposition velocity towards the wall, v_z^+ , was used to demonstrate fibre deposition by either the diffusional or free-flight mechanisms. Results

show that the diffusional deposition mechanism dominates for large t_{res}^+ and small v_z^+ , while the free-flight deposition mechanism is most important for small t_{res}^+ and large v_z^+ . The fibres exhibit orientation anisotropy at impact which is strongly dependent on their elongation. The fibre inertia influences the fibre streakiness, mimicking the viscous sub-layer streaks in a turbulent wall-bounded flow, albeit to a lesser degree due to the external influence of gravity. The fibre inertia was categorised into three groups: low inertia, with $\tau_{ev}^+ = 1$ and 5; intermediate inertia, with $\tau_{ev}^+ = 15$ and 25; and high inertia, with $\tau_{ev}^+ = 50$ and 100. Fibres with low inertia were found to exhibit different deposition behaviour to those with intermediate and high inertia. Overall, the inclusion of particle orientation in the simulations ensures that the deposition patterns of different particles are well captured. Results on the mechanism and pattern of particle deposition reported are of value to subsequent planned research on the effect of particle shape, and fluid and particle inertia, on the particle deposition rate.

Acknowledgements

The authors wish to thank the Engineering and Physical Sciences Research Council for their financial support of the work reported in this paper under EPSRC Grant EP/I003010/1, “Computational Modelling for Advanced Nuclear Power Plants”.

Conflict of Interest

The authors declare that they have no conflicts of interest.

References

1. Hazelton RF. Characteristics of fuel crud and its impact on storage, handling, and shipment of spent fuel: Pacific Northwest Lab;1987. PNL-6273, DE88 000914.
2. Njobuenwu DO, Fairweather M. Modelling of pipe bend erosion by dilute particle suspensions. *Computers & Chemical Engineering*. 2012;42:235-247.
3. Hakansson KO, Kvick M, Lundell F, Prahli Wittberg L, Söderberg LD. Measurement of width and intensity of particle streaks in turbulent flows. *Experiments in Fluids*. 2013;54:1-13.
4. Marchioli C, Soldati A. Mechanisms for particle transfer and segregation in a turbulent boundary layer. *Journal of Fluid Mechanics*. 2002;468:283-315.
5. Liu BYH, Agarwal JK. Experimental observation of aerosol deposition in turbulent flow. *Journal of Aerosol Science*. 1974;5:145-155.
6. Friedlander SK, Johnstone HF. Deposition of suspended particles from turbulent gas streams. *Industrial & Engineering Chemistry*. 1957;49:1151-1156.
7. Narayanan C, Lakehal D, Botto L, Soldati A. Mechanisms of particle deposition in a fully developed turbulent open channel flow. *Physics of Fluids*. 2003;15:763-775.
8. Guha A. Transport and deposition of particles in turbulent and laminar flow. *Annual Review of Fluid Mechanics*. 2008;40:311-341.
9. Dupuy M, Xayasenh A, Duval H, Waz E. Analysis of non-Brownian particle deposition from turbulent liquid-flow. *AIChE Journal*. 2016;62:891-904.
10. Challabotla NR, Zhao L, Andersson HI. On fiber behavior in turbulent vertical channel flow. *Chemical Engineering Science*. 2016;153:75-86.
11. Challabotla NR, Zhao L, Andersson HI. Gravity Effects on Fiber Dynamics in Wall Turbulence. *Flow, Turbulence and Combustion*. 2016:1-16.
12. Uijttewaal WSJ, Oliemans RVA. Particle dispersion and deposition in direct numerical and large eddy simulations of vertical pipe flows. *Physics of Fluids*. 1996;8:2590-2604.

13. Wang Q, Squires KD. Large eddy simulation of particle deposition in a vertical turbulent channel flow. *International Journal of Multiphase Flow*. 1996;22:667-683.
14. Salmanzadeh M, Rahnama M, Ahmadi G. Effect of sub-grid scales on large eddy simulation of particle deposition in a turbulent channel flow. *Aerosol Science and Technology*. 2010;44:796-806.
15. Njobuenwu DO, Fairweather M. Large eddy simulation of non-spherical particle deposition in a vertical turbulent channel flow. In: Jiří Jaromír Klemeš PSV, Peng Yen L, eds. *Computer Aided Chemical Engineering*. Vol Volume 33: Elsevier, 2014:907-912.
16. Kvasnak W, Ahmadi G. Fibrous particle deposition in a turbulent channel flow - An experimental study. *Aerosol Science and Technology*. 1995;23:641-652.
17. Bellani G, Byron ML, Collignon AG, Meyer CR, Variano EA. Shape effects on turbulent modulation by large nearly neutrally buoyant particles. *Journal of Fluid Mechanics*. 2012;712:41-60.
18. Hölzer A, Sommerfeld M. New simple correlation formula for the drag coefficient of non-spherical particles. *Powder Technology*. 2008;184:361-365.
19. Zhang H, Ahmadi G, Fan F-G, McLaughlin JB. Ellipsoidal particles transport and deposition in turbulent channel flows. *International Journal of Multiphase Flow*. 2001;27:971-1009.
20. Mortensen PH, Andersson HI, Gillissen JJJ, Boersma BJ. Dynamics of prolate ellipsoidal particles in a turbulent channel flow. *Physics of Fluids*. 2008;20:093302-093314.
21. Marchioli C, Fantoni M, Soldati A. Orientation, distribution, and deposition of elongated, inertial fibers in turbulent channel flow. *Physics of Fluids*. 2010;22:033301-033314.
22. Tian L, Ahmadi G, Wang Z, Hopke PK. Transport and deposition of ellipsoidal fibers in low Reynolds number flows. *Journal of Aerosol Science*. 2012;45:1-18.
23. Ravnik J, Marchioli C, Hribersek M, Soldati A. On shear lift force modelling for non-spherical particles in turbulent flows. 11th International Conference of Numerical Analysis

- and Applied Mathematics. Vol 1558. Rhodos, Greece: AIP Conference Proceedings Vol. 1558, 2013:1107-1110.
24. Jeffery GB. The motion of ellipsoidal particles immersed in a viscous fluid. Proceedings of the Royal Society of London, Series A. 1922;102:161-179.
 25. Brenner H. The Stokes resistance of an arbitrary particle. Chemical Engineering Science. 1963;18:1-25.
 26. Brenner H. The Stokes resistance of an arbitrary particle - IV Arbitrary fields of flow. Chemical Engineering Science. 1964;19:703-727.
 27. Zastawny M, Mallouppas G, Zhao F, van Wachem B. Derivation of drag and lift force and torque coefficients for non-spherical particles in flows. International Journal of Multiphase Flow. 2012;39:227-239.
 28. Ganser GH. A rational approach to drag prediction of spherical and nonspherical particles. Powder Technology. 1993;77:143-152.
 29. Rosendahl L. Extending the modelling framework for gas-particle systems: Applications of multiparameter shape descriptions to non-conventional solid fuels in reacting and non-reacting environments. PhD Thesis. Denmark, Aalborg University; 1998.
 30. Ouchene R, Khalij M, Arcen B, Tanière A. A new set of correlations of drag, lift and torque coefficients for non-spherical particles and large Reynolds numbers. Powder Technology. 2016;303:33-43.
 31. Mandø M, Rosendahl L. On the motion of non-spherical particles at high Reynolds number. Powder Technology. 2010;202:1-13.
 32. Yin C, Rosendahl L, Knudsen Kær S, Sørensen H. Modelling the motion of cylindrical particles in a nonuniform flow. Chemical Engineering Science. 2003;58:3489-3498.
 33. Hölzer A, Sommerfeld M. Lattice Boltzmann simulations to determine drag, lift and torque acting on non-spherical particles. Computers & Fluids. 2009;38:572-589.
 34. Njobuenwu DO, Fairweather M. Simulation of inertial fibre orientation in turbulent flow. Physics of Fluids. 2016;28:063307.

35. Njobuenwu DO, Fairweather M. Large eddy simulation of deposition of anisotropic particles in a turbulent channel flow. 10th International ERCOFTAC Symposium on Engineering Turbulence Modelling and Measurements; 17-19 September, 2014; Marbella, Spain.
36. Piomelli U, Liu J. Large-eddy simulation of rotating channel flows using a localized dynamic model. *Physics of Fluids*. 1995;7:839-848.
37. Bini M, Jones WP. Large-eddy simulation of particle-laden turbulent flows. *Journal of Fluid Mechanics*. 2008;614:207-252.
38. Jiang F, Gallardo JP, Andersson HI. The laminar wake behind a 6:1 prolate spheroid at 45° incidence angle. *Physics of Fluids*. 2014;26:113602.
39. Crowe CT, Troutt TR, Chung JN. Numerical models for two-phase turbulent flows. *Annual Review of Fluid Mechanics*. 1996;28:11-43.
40. Fan F-G, Ahmadi G. A sublayer model for wall deposition of ellipsoidal particles in turbulent streams. *Journal of Aerosol Science*. 1995;26(5):813-840.
41. Njobuenwu DO, Fairweather M. Dynamics of single, non-spherical ellipsoidal particles in a turbulent channel flow. *Chemical Engineering Science*. 2015;123:265-282.
42. Njobuenwu DO, Fairweather M. Effect of shape on inertial particle dynamics in a channel flow. *Flow, Turbulence and Combustion*. 2014;92:83-101.
43. Marchioli C, Soldati A. Reynolds number scaling of particle preferential concentration in turbulent channel flow. In: Palma JMLM, Lopes AS, eds. *Advances in Turbulence XI*. Vol 117: Springer Berlin Heidelberg, 2007:298-300.
44. Zhang H, Ahmadi G, Asgharian B. Transport and deposition of angular fibers in turbulent channel flows. *Aerosol Science and Technology*. 2007;41:529-548.

List of Table Captions

Table 1: Fibre simulation parameters. All fibre sets have the same density ratio, $\Phi_p = 770$.

Bold values are for fibres with $c^+ > 5$, beyond the viscous sub-layer.

List of Figure Captions

Fig. 1: (a) Relationship between the inertial $\mathbf{x} = [x, y, z]$, the particle $\mathbf{x}' = [x', y', z']$ and the co-moving $\mathbf{x}'' = [x'', y'', z'']$ coordinate systems and definition of the Euler angles (φ, θ, ψ) . $N = \text{plane}[x', y'] \cap \text{plane}[x'', y'']$. θ is the angle between the z' -axis and z'' , φ is the angle between the x'' -axis and N , and ψ is the angle between the x' -axis and N ; (b) Illustration of the location of the centres of gravity (CG) and pressure (CP), the incident angle α_i and the forces acting on the particle. x_{cp} is the distance between CG and CP; (c) Angles θ_x , θ_y and θ_z are, respectively, the angles between the particle principal axis z' and its co-moving axes x'' , y'' and z'' .

Fig. 2: (a) Non-dimensional mean streamwise fluid velocity, u_z^+ , and (b) non-dimensional wall-normal ($u_{x,rms}^+$), spanwise ($u_{y,rms}^+$) and streamwise ($u_{z,rms}^+$) root mean square of velocity fluctuations and shear stress ($u_x^+ u_z^+$) at $Re_\tau = 300$.

Fig. 3: Spatial and orientational distribution of 3500 fibres deposited on the $(y-z)$ plane of the channel for fibres with parametrical scales $(\tau_{ev}^+, \lambda) =$ (a) (5,10), (b) (25,3) and (c) (25,10). The shape represents the fibre orientation while the colour map represents the absolute value of the direction cosine of the angle between the fibre principal axis, z' , and the wall-normal direction, x -axis, $(|\cos\theta_x|)$.

Fig. 4: Effect of fibre elongation ($\lambda=1.001, 3, 10, 30$ and 50) and inertia on PDF of particle wall-normal position at impact normalised with the particle semi-minor length and semi-major length, $(x-a)/(c-a)$, for a range of non-dimensional particle response times: $\tau_{ev}^+ =$ (a) 1, (b) 5, (c) 15, (d) 25, (e) 50 and (f) 100.

Fig. 5: Effect of fibre elongation ($\lambda=1.001, 3, 10, 30$ and 50) and inertia on PDF of non-dimensional particle velocity at impact, v_z^+ , for a range of non-dimensional particle response times: $\tau_{ev}^+ =$ (a) 1, (b) 5, (c) 15, (d) 25, (e) 50 and (f) 100.

Fig. 6: Effect of fibre elongation ($\lambda=1.001, 3, 10, 30$ and 50) and inertia on PDF of non-dimensional particle residence time, t_{res}^+ , in the region $x^+ < 5$ for a range of non-dimensional particle response times: $\tau_{ev}^+ =$ (a) 1, (b) 5, (c) 15, (d) 25, (e) 50 and (f) 100.

Fig. 7: Effect of fibre elongation ($\lambda=1.001, 3, 10, 30$ and 50) and inertia on PDF of absolute direction cosine, $|\cos\theta_x|$, between particle principal axis, z' , and global x -axis for a range of non-dimensional particle response times: $\tau_{ev}^+ =$ (a) 1, (b) 5, (c) 15, (d) 25, (e) 50 and (f) 100.

Fig. 8: Effect of fibre elongation ($\lambda=1.001, 3, 10, 30$ and 50) and inertia on PDF of absolute direction cosine, $|\cos\theta_y|$, between particle principal axis, z' , and global y -axis for a range of non-dimensional particle response times: $\tau_{ev}^+ =$ (a) 1, (b) 5, (c) 15, (d) 25, (e) 50 and (f) 100.

Fig. 9: Effect of fibre elongation ($\lambda=1.001, 3, 10, 30$ and 50) and inertia on PDF of absolute direction cosine, $|\cos\theta_z|$, between particle principal axis, z' , and global z -axis for a range of non-dimensional particle response times: $\tau_{ev}^+ =$ (a) 1, (b) 5, (c) 15, (d) 25, (e) 50 and (f) 100.

Tables

Table 1: Fibre simulation parameters. All fibre sets have the same density ratio, $\Phi_\rho = 770$.

Bold values are for fibres with $c^+ > 5$, beyond the viscous sub-layer.

λ	$r_{ev}^+ = 1$ $d_{ev}^+ = 0.15$		$r_{ev}^+ = 5$ $d_{ev}^+ = 0.34$		$r_{ev}^+ = 15$ $d_{ev}^+ = 0.59$		$r_{ev}^+ = 25$ $d_{ev}^+ = 0.76$		$r_{ev}^+ = 50$ $d_{ev}^+ = 1.08$		$r_{ev}^+ = 100$ $d_{ev}^+ = 1.53$	
	a^+	c^+	a^+	c^+	a^+	c^+	a^+	c^+	a^+	c^+	a^+	c^+
1.001	0.08	0.08	0.17	0.17	0.30	0.30	0.38	0.38	0.54	0.54	0.76	0.77
3	0.05	0.16	0.12	0.36	0.21	0.62	0.27	0.80	0.37	1.12	0.53	1.59
10	0.04	0.35	0.08	0.79	0.14	1.37	0.18	1.77	0.25	2.51	0.35	3.55
30	0.02	0.74	0.06	1.65	0.10	2.86	0.12	3.69	0.17	5.22	0.25	7.38
50	0.02	1.04	0.05	2.32	0.08	4.02	0.10	5.19	0.15	7.34	0.21	10.38

Figures

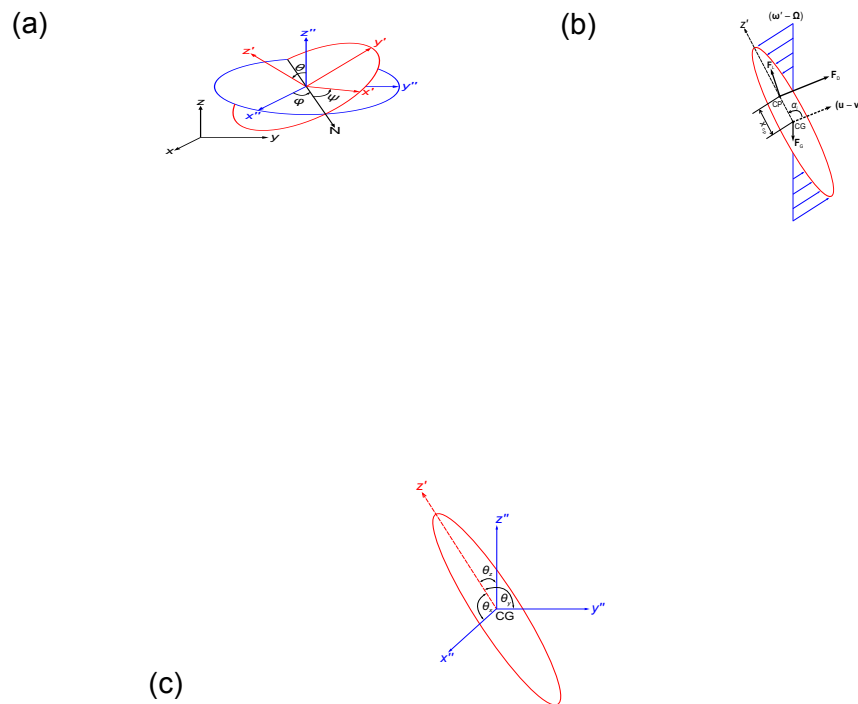


Fig. 1: (a) Relationship between the inertial $\mathbf{x} = [x, y, z]$, the particle $\mathbf{x}' = [x', y', z']$ and the co-moving $\mathbf{x}'' = [x'', y'', z'']$ coordinate systems and definition of the Euler angles (φ, θ, ψ) . $N = \text{plane}[x', y'] \cap \text{plane}[x'', y'']$. θ is the angle between the z' -axis and z'' , φ is the angle between the x' -axis and N , and ψ is the angle between the x' -axis and z'' ; (b) Illustration of the location of the centres of gravity (CG) and pressure (CP), the incident angle α_i and the forces acting on the particle. x_{cp} is the distance between CG and CP; (c) Angles θ_x , θ_y and θ_z are, respectively, the angles between the particle principal axis z' and its co-moving axes x'' , y'' and z'' .

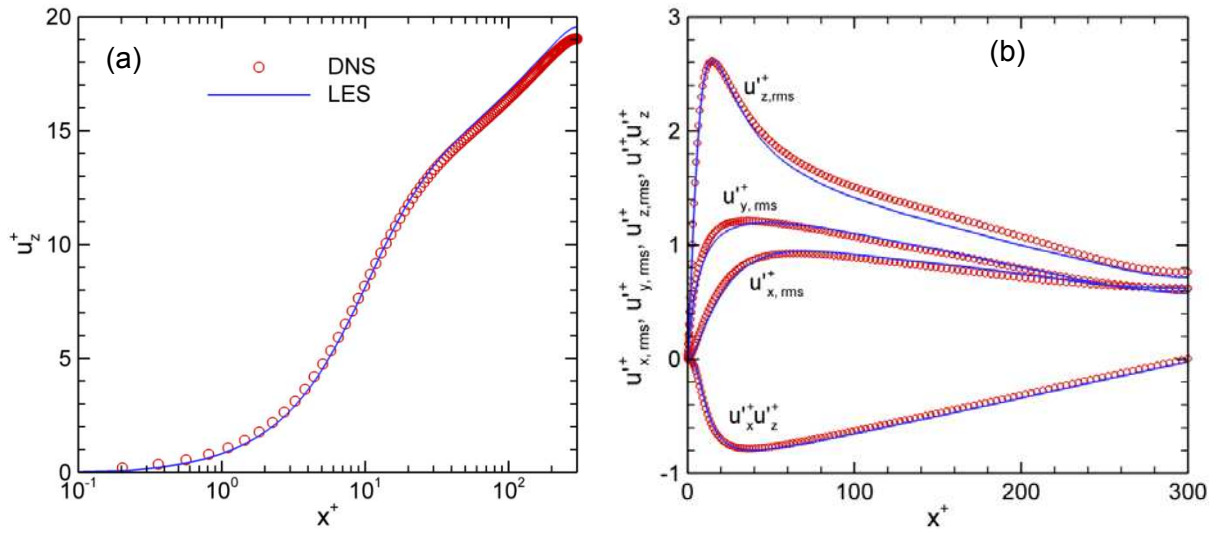


Fig. 2: (a) Non-dimensional mean streamwise fluid velocity, u_z^+ , and (b) non-dimensional wall-normal ($u_{x,rms}^+$), spanwise ($u_{y,rms}^+$) and streamwise ($u_{z,rms}^+$) root mean square of velocity fluctuations and shear stress ($u_x^+ u_z^+$) at $Re_\tau = 300$.

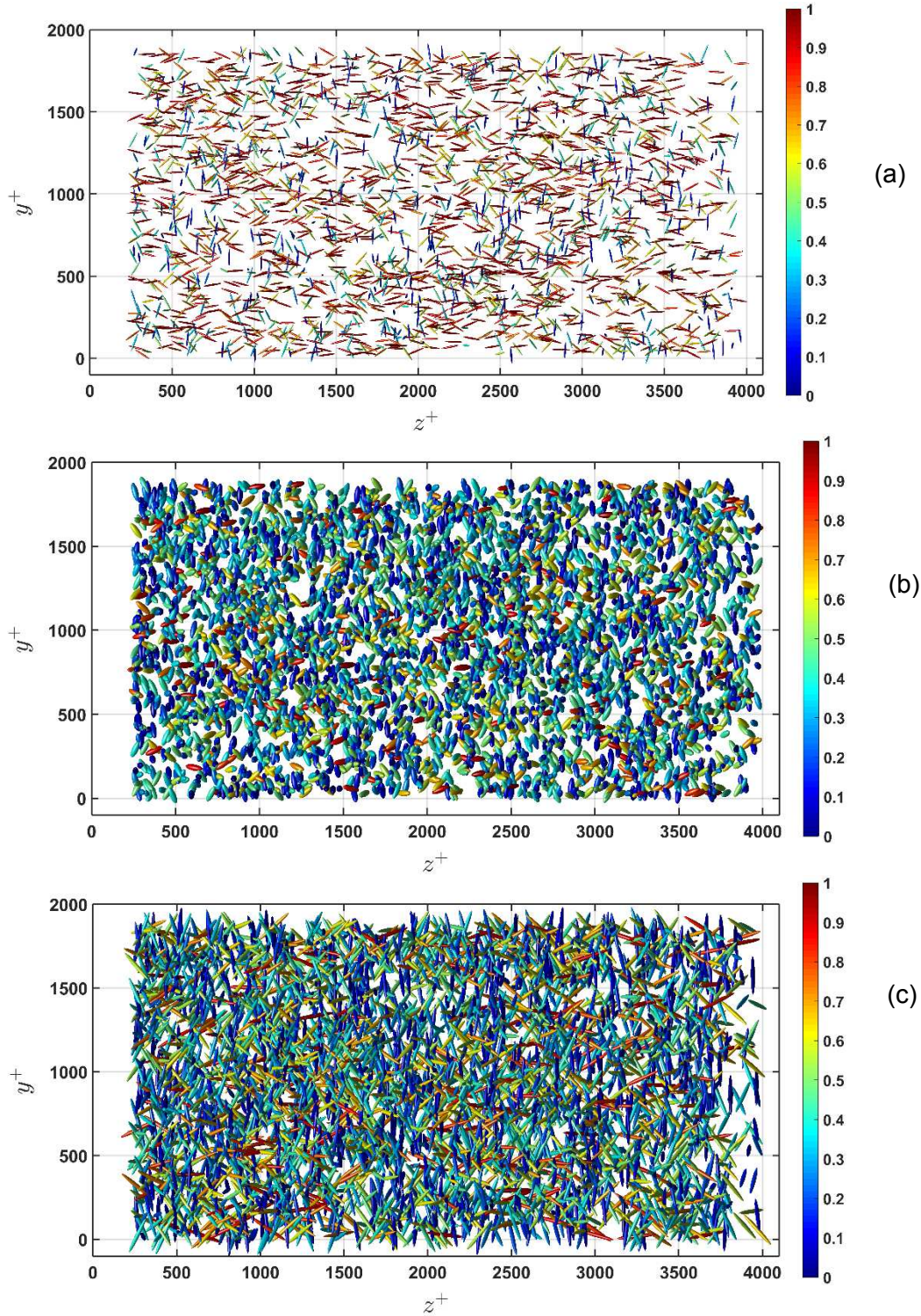


Fig. 3: Spatial and orientational distribution of 3500 fibres deposited on the (y - z) plane of the channel for fibres with parametrical scales $(\tau_{ev}^+, \lambda) =$ (a) (5,10), (b) (25,3) and (c) (25,10). The shape represents the fibre orientation while the colour map represents the absolute value of the direction cosine of the angle between the fibre principal axis, z' , and the wall-normal direction, x -axis, ($|\cos\theta_x|$).

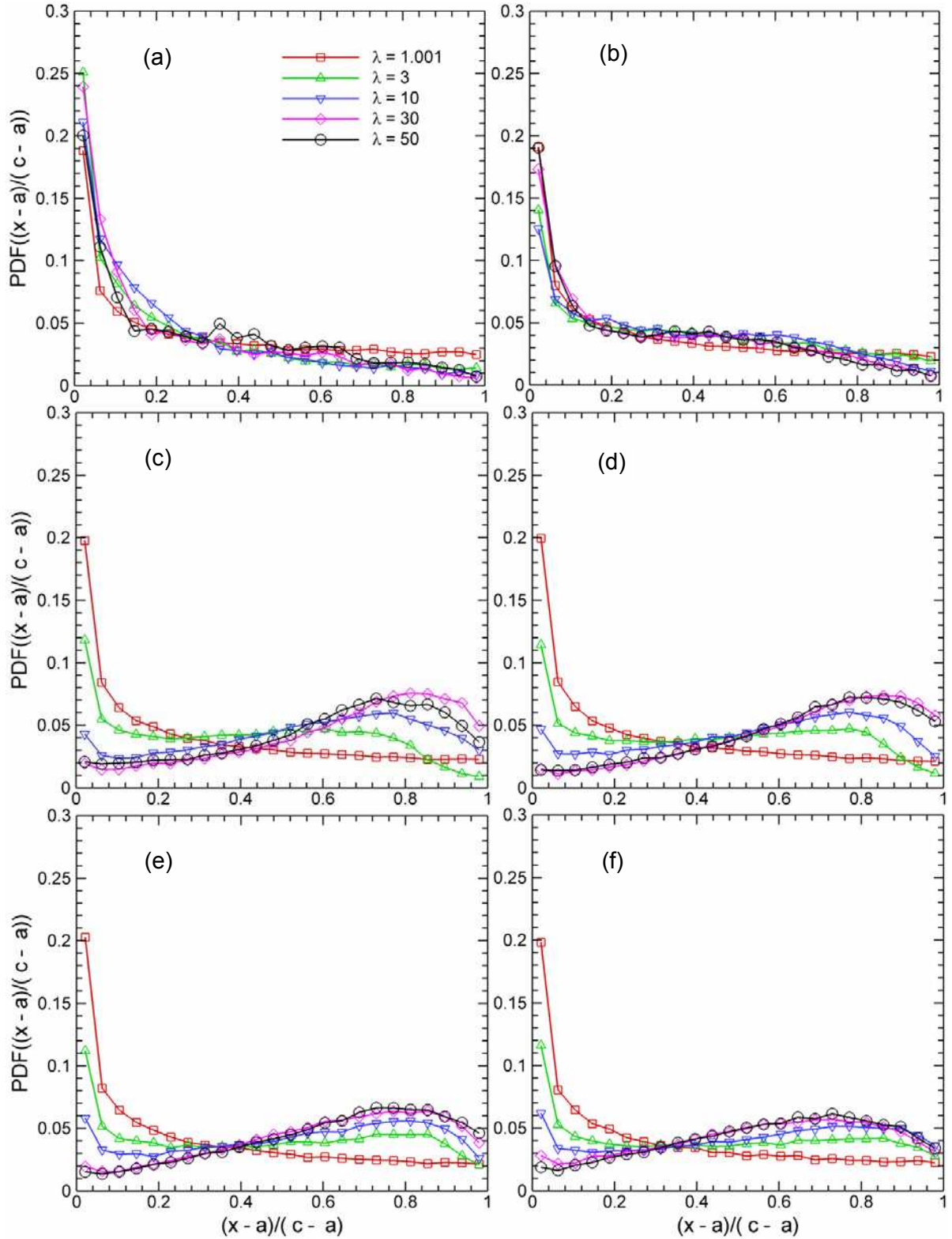


Fig. 4: Effect of fibre elongation ($\lambda=1.001, 3, 10, 30$ and 50) and inertia on PDF of particle wall-normal position at impact normalised with the particle semi-minor length and semi-major length, $(x - a)/(c - a)$, for a range of non-dimensional particle response times: $\tau_{ev}^+ =$ (a) 1, (b) 5, (c) 15, (d) 25, (e) 50 and (f) 100.

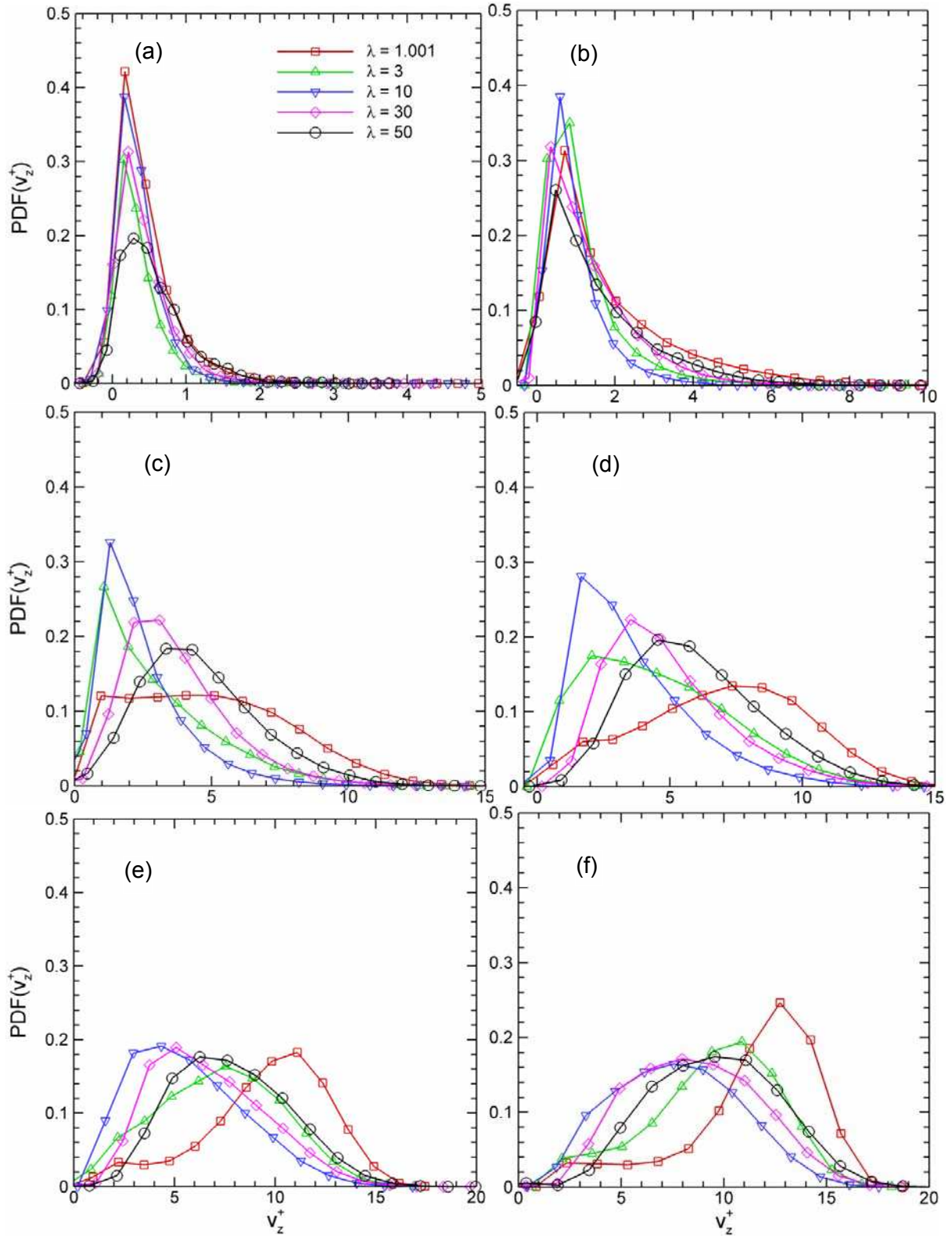


Fig. 5: Effect of fibre elongation ($\lambda=1.001, 3, 10, 30$ and 50) and inertia on PDF of non-dimensional particle wall-normal velocity at impact, v_z^+ , for a range of non-dimensional particle response times: $\tau_{ev}^+ =$ (a) 1, (b) 5, (c) 15, (d) 25, (e) 50 and (f) 100.

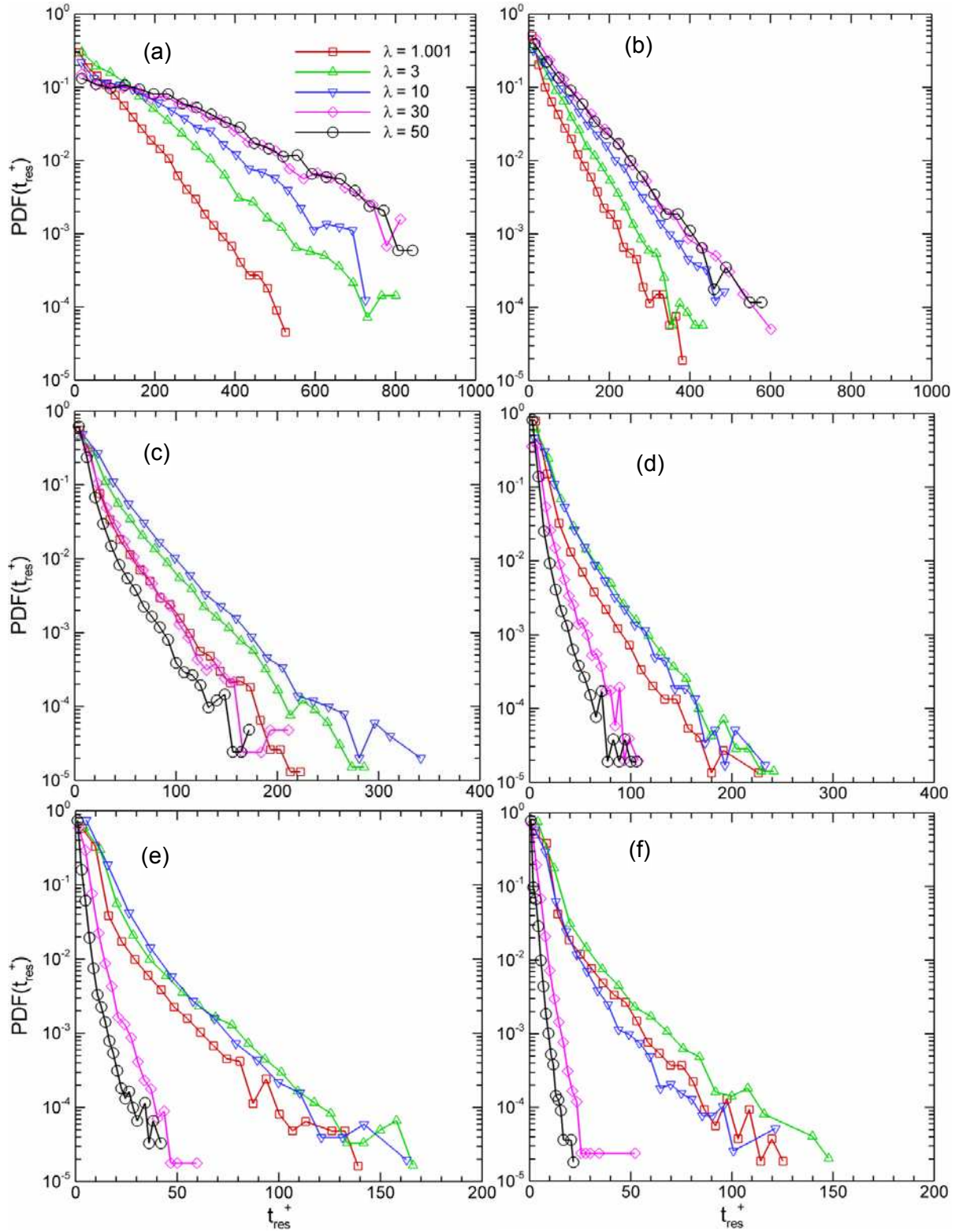


Fig. 6: Effect of fibre elongation ($\lambda=1.001, 3, 10, 30$ and 50) and inertia on PDF of non-dimensional particle residence time, t_{res}^+ , in the region $x^+ < 5$ for a range of non-dimensional particle response times: $\tau_{ev}^+ =$ (a) 1, (b) 5, (c) 15, (d) 25, (e) 50 and (f) 100.

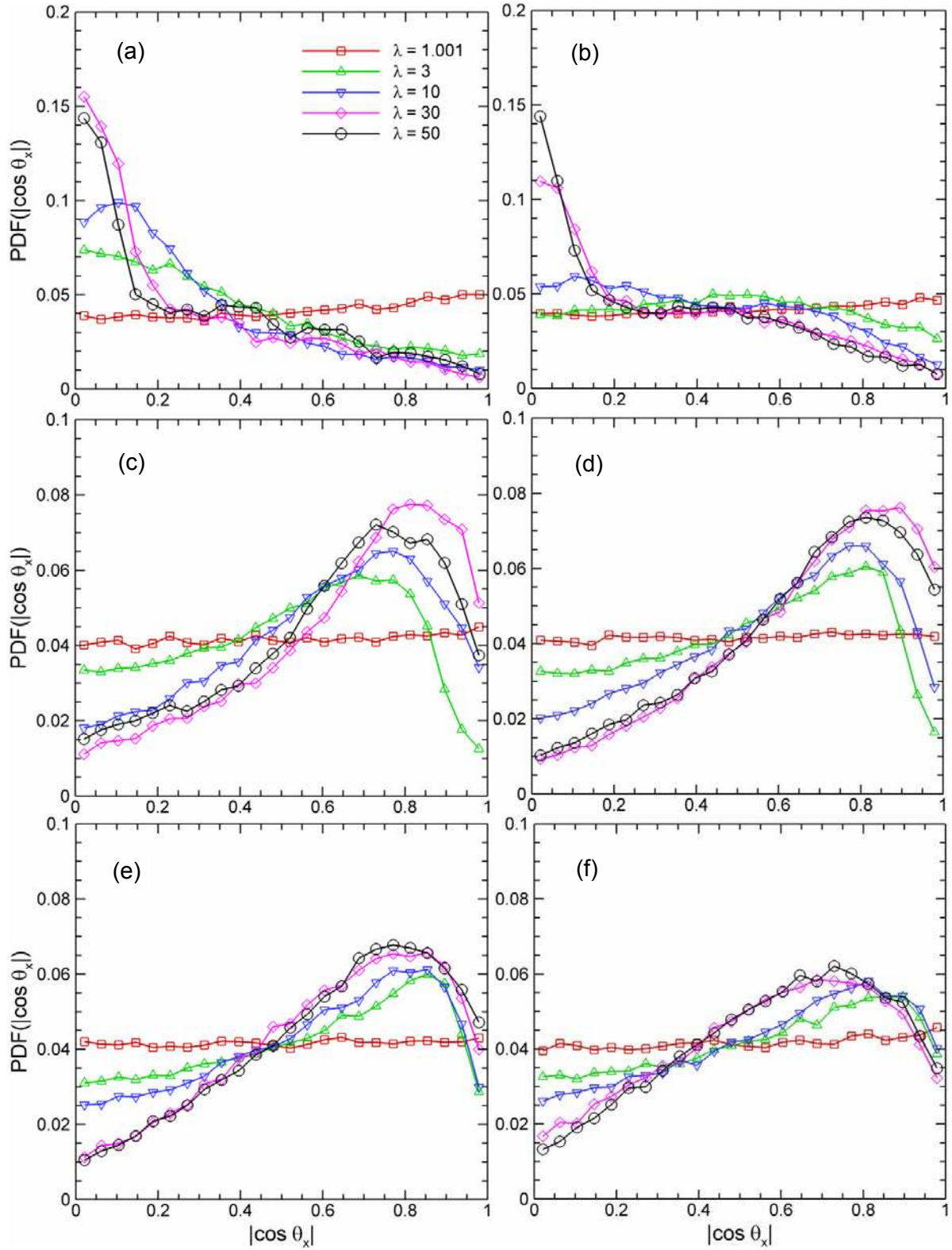


Fig. 7: Effect of fibre elongation ($\lambda=1.001, 3, 10, 30$ and 50) and inertia on PDF of absolute direction cosine, $|\cos \theta_x|$, between particle principal axis, z' , and global x -axis for a range of non-dimensional particle response times: $\tau_{ev}^+ =$ (a) 1, (b) 5, (c) 15, (d) 25, (e) 50 and (f) 100.

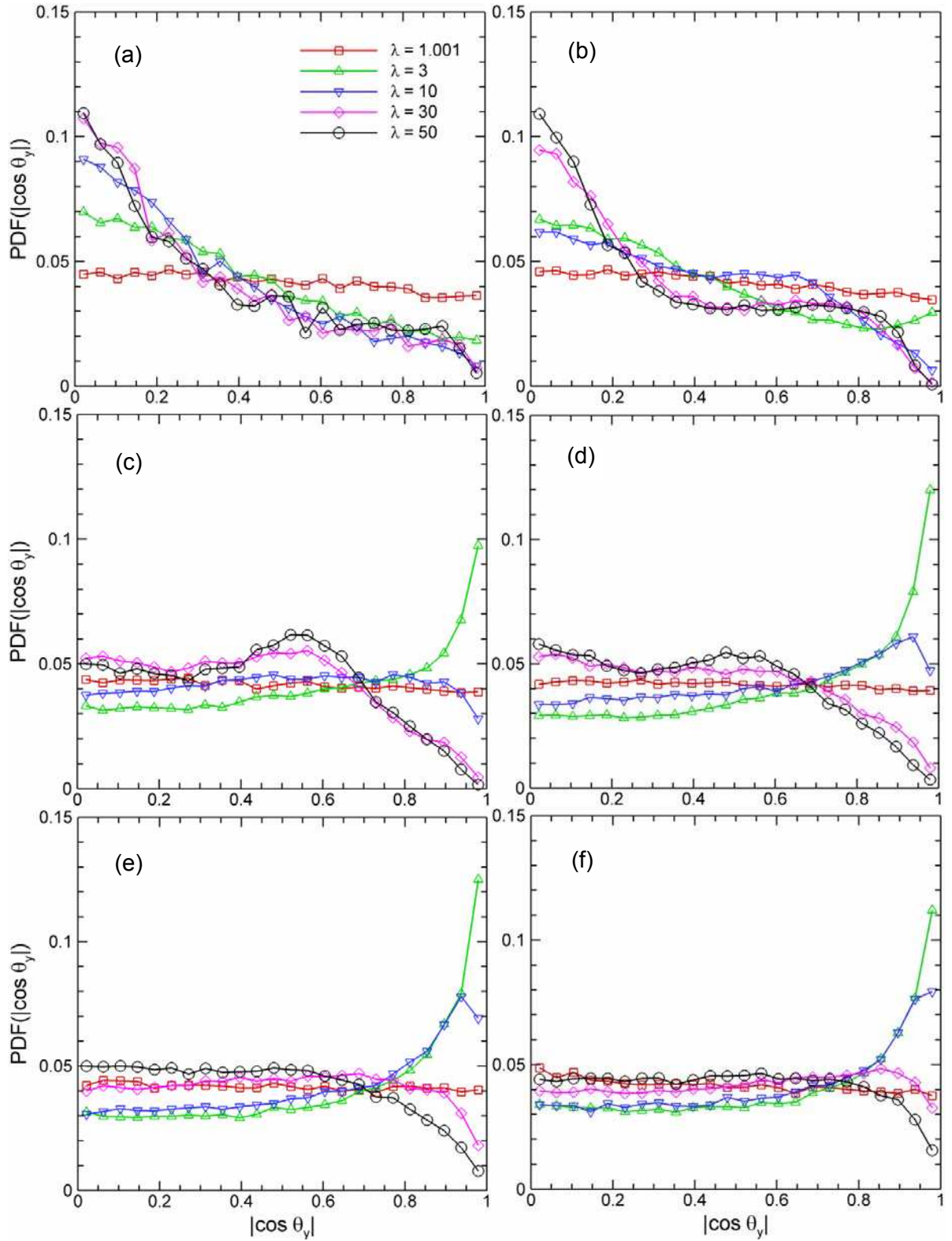


Fig. 8: Effect of fibre elongation ($\lambda = 1.001, 3, 10, 30$ and 50) and inertia on PDF of absolute direction cosine, $|\cos \theta_y|$, between particle principal axis, z' , and global y -axis for a range of non-dimensional particle response times: $\tau_{ev}^+ =$ (a) 1, (b) 5, (c) 15, (d) 25, (e) 50 and (f) 100.

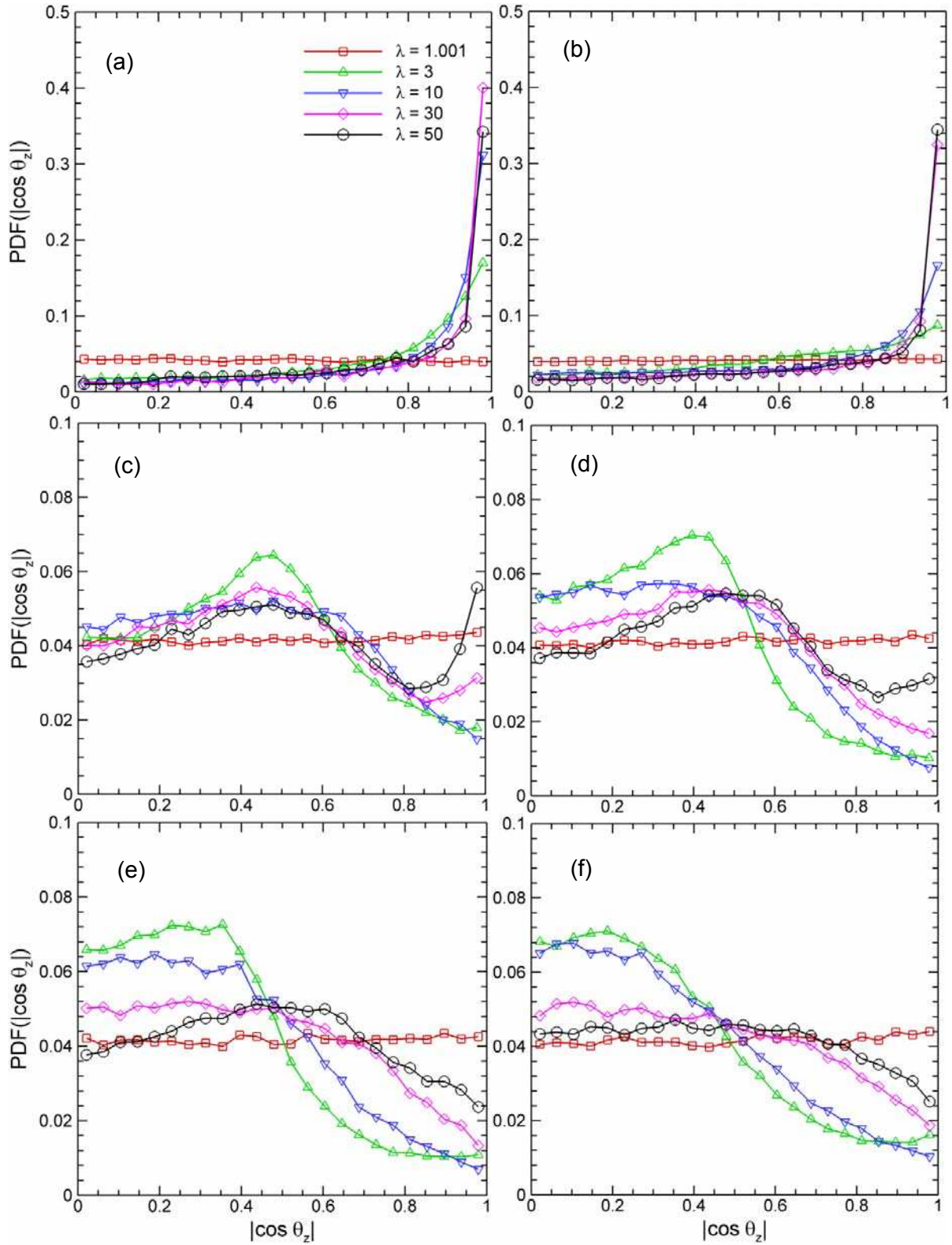


Fig. 9: Effect of fibre elongation ($\lambda = 1.001, 3, 10, 30$ and 50) and inertia on PDF of absolute direction cosine, $|\cos \theta_z|$, between particle principal axis, z' , and global z -axis for a range of non-dimensional particle response times: $\tau_{ev}^+ =$ (a) 1, (b) 5, (c) 15, (d) 25, (e) 50 and (f) 100.